

# Multifunctional P-doped TiO<sub>2</sub> Films: A New Approach to Self-Cleaning, Transparent Conducting Oxide Materials.

Carlos Sotelo-Vazquez<sup>†</sup>, Nuruzzaman Noor<sup>†</sup>, Andreas Kafizas<sup>†‡</sup>, Raul Quesada-Cabrera<sup>†</sup>, David O. Scanlon<sup>δ‡</sup>, Alaric Taylor<sup>‡</sup>, James R. Durrant<sup>‡</sup> and Ivan P. Parkin<sup>†\*</sup>

<sup>†</sup>Materials Chemistry Research Centre, Department of Chemistry, University College London, 20 Gordon St., London, WC1H 0AJ, United Kingdom. [i.p.parkin@ucl.ac.uk](mailto:i.p.parkin@ucl.ac.uk)

<sup>‡</sup>Department of Chemistry, Imperial College London, Exhibition Road, London, SW7 2AZ, United Kingdom.

<sup>δ</sup>University College London, Kathleen Lonsdale Materials Chemistry, Department of Chemistry, 20 Gordon St, London WC1H 0AJ, United Kingdom

<sup>‡</sup>Diamond Light Source Ltd., Diamond House, Harwell Science and Innovation Campus, Didcot, Oxfordshire OX11 0DE, United Kingdom.

<sup>‡</sup>Department of Electronic & Electrical Engineering, University College London, Torrington Place, London, WC1E 7JE

**KEYWORDS:** cation-anion phosphorus doping, titanium dioxide (TiO<sub>2</sub>), transparent conducting oxide (TCO), transient absorption spectroscopy (TAS), chemical vapour deposition (CVD).

---

**ABSTRACT:** Multifunctional P-doped TiO<sub>2</sub> thin-films were synthesised by atmospheric pressure chemical vapour deposition (APCVD). This is the first example of P-doped TiO<sub>2</sub> films with both P<sup>5+</sup> and P<sup>3-</sup> states, with the relative proportion being determined by synthesis conditions. This technique to control the oxidation state of the impurities presents a new approach to achieve films with both self-cleaning and TCO properties. The origin of electrical conductivity in these materials was correlated to the incorporation of P<sup>5+</sup> species, as suggested by Hall Effect probe measurements. The photocatalytic performance of the films was investigated using the model organic pollutant, stearic acid, with films containing predominately P<sup>3-</sup> states found to be vastly inferior photocatalysts compared to undoped TiO<sub>2</sub> films. Transient absorption spectroscopy studies also showed that charge carrier concentrations increased by several orders of magnitude in films containing P<sup>5+</sup> species only, whereas photo-generated carrier lifetimes – and thus photocatalytic activity, were severely reduced upon incorporation of P<sup>3-</sup> species. The results presented here provide important insights on the influence of dopant nature and location within a semiconductor structure. These new P-doped TiO<sub>2</sub> films are a breakthrough in the development of multifunctional advanced materials with tuned properties for a wide range of applications.

---

## 1. INTRODUCTION

Titania (TiO<sub>2</sub>) is the most widely studied photocatalytic material as it is highly active, durable to extended photocatalytic cycling, mechanically robust and largely chemically inert over a wide range of pH and voltage. TiO<sub>2</sub> has been extensively used in different photocatalytic applications, including water and air-purification, water splitting, self-cleaning materials and for the degradation of cancer cells and viruses.<sup>1-4</sup> However, the band-gap of TiO<sub>2</sub> (anatase phase  $\approx$  3.2 eV) lies in the UV region of the electromagnetic spectrum, which minimises its maximum solar efficiency. This has led to a large research drive to develop doping strategies in an effort to decrease the band gap of TiO<sub>2</sub>.

Non-metal acceptor doping has been extensively employed to extend the absorption properties of TiO<sub>2</sub> into the visible range. This type of doping should simultaneously raise the valence band maximum of TiO<sub>2</sub> (causing a redshift of the absorption edge) and reduce the number of recombination centres,<sup>5</sup> with nitrogen being the most commonly studied dopant. Despite the wealth of literature on N-doped TiO<sub>2</sub>,<sup>6</sup> there is little consensus on whether this leads to an overall improvement in sunlight driven photocatalysis.<sup>7-12</sup>

Cationic dopants with a higher oxidation state than Ti<sup>4+</sup> do not reduce the visible light response of anatase TiO<sub>2</sub>. Instead they act as electron donors, injecting electrons into the conduction band, and can transform anatase into a transparent conducting oxide (TCO). This transformation normally occurs with a blue shift of the optical absorption, and a dramatic reduction in resistivity, with typical donor dopants being Nb, Ta and W.<sup>13-15</sup> The use of TiO<sub>2</sub>-based materials for TCO applications presents advantages compared to indium-based TCO materials; such as high refractive index, high transmittance in the infrared region and high chemical stability as well as a significant reduction in the production cost.<sup>16</sup> Ta and Nb doping show electrical and optical properties comparable to ITO materials; however, W and F doping do not yield low enough resistivities, which could be attributed to a charge carrier concentration effect (*ie.* lower donation efficiency).<sup>17</sup> In all cases, however, a penalty in terms of reduced photocatalytic performance must often be paid.

The choice of phosphorous as a dopant allows the possibility of both cationic (P<sup>5+</sup>) and anionic (P<sup>3-</sup>) doping of anatase TiO<sub>2</sub>. In the pentavalent state (P<sup>5+</sup>), phosphorous can induce a blue-shift and an increase in the free charge carriers of phosphorous-doped TiO<sub>2</sub> films. In addition, P is a much cheaper and more

earth abundant dopant than either Nb or Ta, and so represents an attractive alternative with a view to large scale industrial deployment. Therefore, the synthesis of phosphorus-doped films could present a new approach to produce TCO materials. To the best of our knowledge, the electrical properties of phosphorus-doped TiO<sub>2</sub> films are yet to be studied.

Phosphorus-doped TiO<sub>2</sub> films (henceforth, P-TiO<sub>2</sub>) have been previously synthesised via the sol-gel method. These P-doped materials were reported to possess a single oxidation state assigned to a phosphate state (P<sup>5+</sup>).<sup>18-21</sup> Different methods such as degradation of dyes (methyl orange (MO) and methylene blue (MB)) and organic compounds (*n*-pentane and ethanol) were performed to assess the photocatalytic activity of the samples. These tests showed different photocatalytic values, which could be attributed to varying phosphate content and surface area of the samples.

In the present work, APCVD was used to produce high quality P-TiO<sub>2</sub> films.<sup>22</sup> This method presents advantages over the sol-gel route, as the material is grown directly at high temperature. This avoids the amorphous to crystalline transition imposed in sol-gel that could drastically alter the nature and content of the dopant.<sup>18-20</sup> Interestingly, our CVD route can achieve multi-valent P-doping, where cationic P<sup>3+</sup> and anionic P<sup>3-</sup> are present.<sup>7</sup> This paper explores the nature and effect of P-doping TiO<sub>2</sub> thin-films on the electronic and photocatalytic functionality.

## 2. EXPERIMENTAL SECTION

All chemicals were purchased from *Sigma-Aldrich*. Titanium tetrachloride (TiCl<sub>4</sub>, 99.9 %), ethyl acetate (C<sub>4</sub>H<sub>8</sub>O<sub>2</sub>, 99.8 %) and tri-ethyl phosphate ((C<sub>2</sub>H<sub>5</sub>O)<sub>3</sub>PO, 99.8 %) were used as titanium, oxygen and phosphorus sources, respectively. Octadecanoic (stearic) acid (CH<sub>3</sub>(CH<sub>2</sub>)<sub>15</sub>CH<sub>2</sub>CO<sub>2</sub>, 98.5%) was used to perform the photocatalytic test.

### 2.1. Atmospheric Pressure Chemical Vapour Deposition Apparatus

The whole CVD apparatus was kept at high temperature (473 K). The precursors were heated independently in stainless steel bubblers in order to generate enough vapour pressure to be carried into the reactor. Pre-heated nitrogen (473 K) was used as the carrier gas (supplied by BOC), to drag the precursor vapours into stainless steel mixing chambers kept at 523 K, under controlled flow rate conditions. A plain nitrogen flow pushed the gas mixture through a triple baffle manifold that produced wide laminar flow into the reactor. The reactor consisted of a graphite block (320 mm-long x 150 mm-width) contained within a quartz glass tube and heated using three embedded *Whatman* heater cartridges. The temperature was controlled using Pt-Rh thermocouples.

Films were grown at 773 K on float glass substrates (89 x 225 x 4 mm) supplied by the *Pilkington NSG Group*, which is pre-coated with a SiO<sub>2</sub> barrier layer to prevent ion diffusion from the glass into the film. The glass substrates were thoroughly cleaned using acetone (99 %), isopropanol (99.9 %) and distilled water and dried in air prior to use.

### 2.2. Analytical Methods

X-ray diffraction (XRD) analysis was performed using a Bruker-Axs D8 (Lynxeye XE) diffractometer. The instrument operates with a Cu X-ray source, monochromated (K $\alpha_1$ , 1.54 Å). Films were analysed with a glancing incident angle ( $\theta$ ) of 1°. Le Bail fits were made to the diffraction patterns, using the anatase structure parameters from Joint Committee on Powder Diffraction Standards (JCPDS), through the GSAS and EXPGUI software suite. UV/vis spectroscopy was performed using a double monochromated Perkin Elmer Lambda 950 UV/Vis/NIR Spectrophotometer in the 300 – 2500 nm range. Reflectance spectra was recorded for different positions in the range 300 – 2500 nm on a Helios double beam instrument standardised relative to a silicon mirror, which allowed the thickness of the films to be determined via *Swanepoel* method.<sup>23</sup> The latter measurements were confirmed for selected samples using side-view scanning electron microscopy (SEM). The SEM studies were carried out using a JEOL 6301 (5 KV) and a JEOL JSM-6700F field emission instruments and the Oxford software INCA was used by EDX. Atomic force microscopy (AFM) was conducted using a Bruker Icon system running in PeakForce Quantitative Nanomechanical Property Mapping (QNM) mode. Bruker NCHV (etched silicon) tips were used in contact mode over a selection of 5  $\mu\text{m}$  x 5  $\mu\text{m}$  areas to measure the topography of the samples. X-Ray photoelectron spectroscopy (XPS) was performed using a Thermo K alpha spectrometer with monochromated Al K alpha radiation, a dual beam charge compensation system and constant pass energy of 50 eV. Survey scans were collected in the range of 0 – 1200 eV. High-resolution peaks were used for the principal peaks of Ti (2p), O (1s), P (2p), C (1s) and Si (2p). The peaks were modeled using relative sensitivity factors to calculate the film composition. The area underneath these bands is an indication of the concentration of element within the region of analysis (spot size 400  $\mu\text{m}$ ).

### 2.3. Transient absorption spectroscopy

Charge carrier dynamics of TiO<sub>2</sub> films were measured using transient absorption spectroscopy (TAS) from the  $\mu\text{s}$  – s time-scale at room temperature ( $\approx$  297 K). The TAS apparatus has been described in detail elsewhere.<sup>24</sup> In brief, a 75 W Xe lamp is used as a probe beam with a monochromator placed before the sample. The change in transmitted light is measured by a Si PIN photodiode after a UV laser excitation pulse is applied on the sample using the third harmonic of an Nd: YAG laser (355 nm, 6 ns pulse width). Reasonably low laser intensities were used ( $\approx$  500  $\mu\text{J cm}^{-2}$  pulse<sup>-1</sup>) with a laser repetition rate of 1 Hz. Each TAS trace is the result of averaging between 50 and 500 scans.

### 2.4. Hall Effect

Hall Effect probe measurements were conducted at room temperature on an Ecopia HMS-3000 device in the Van der Pauw configuration. Measurements were acquired at 0.58 T with a variable current of 1  $\mu\text{A}$  – 300  $\mu\text{A}$ , on square cut samples with

soldered indium-tin ohmic contacts, the integrity of which were tested prior to measurement.

### 2.5. Photocatalytic test

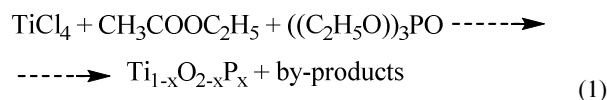
The photocatalytic performance of the films synthesised in this work was evaluated during photodegradation of octadecanoic (stearic) acid (95 %, *Sigma-Aldrich*). Films were dip-coated with a thin layer of stearic acid using a 0.05 M solution in chloroform. The photocatalytic activity of samples was measured under either UVA (*Vilber-Lourmat*, 2 x 8 W, 365 nm, 1.2 mW cm<sup>-2</sup>) illumination. A Perkin Elmer RX-I Fourier transform infrared (FTIR) spectrometer was used to monitor the degradation of the overlain stearic acid.

The integrated areas between the characteristic C-H infrared bands at 2958, 2923 and 2853 cm<sup>-1</sup> were calculated. The photoactivity rates were estimated from linear regression of the initial 30 – 40 % of the degradation, where the reaction has been shown to possess zero-order reaction kinetics above a critical stearic acid concentration. Using a conversion factor, the number of molecules of stearic acid degraded was estimated considering that 1 cm<sup>-1</sup> of integrated area correspond to 9.7 x 10<sup>15</sup> molecules of stearic acid.<sup>25</sup> Formal quantum efficiencies (FQE), defined as molecules of acid degraded per incident photon (molec photon<sup>-1</sup>) were calculated assuming all incident photons had the same energy (3.4 eV) and were absorbed by the films.

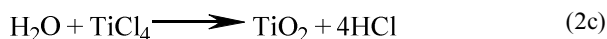
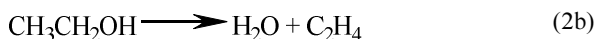
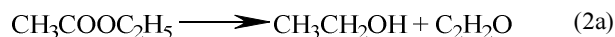
## 3. RESULTS AND DISCUSSION

### 3.1. Films Synthesis

Phosphorus-doped TiO<sub>2</sub> thin-films were grown on glass by APCVD, from the reaction of titanium tetrachloride (TiCl<sub>4</sub>), ethyl acetate (EtOAc) and tri-ethyl phosphate ((EtO)<sub>3</sub>PO) at 773 K, following Equation (1).



The particular reaction mechanism between TiCl<sub>4</sub> and EtOAc is not known. A possible mechanism involves the hydrolysis of TiCl<sub>4</sub> (Equation 2)<sup>26</sup> via decomposition of ethyl acetate to form ketene and ethanol and subsequent dehydration of ethanol to form ethene and water.



In phosphorus doping, the vapour pressure of the phosphorus source was controlled by heating the stainless steel bubbler to 363 K. Film thickness (as determined from side-on SEM and

the optical Swanepoel method)<sup>23</sup> varied between 450-1050 nm depending on the precursors flow rate. This variation in the thickness across the substrate corresponds to the presence of optical interference, each colour band corresponding to a different region of thickness.<sup>27</sup> The corresponding flow rates and phosphorus content are listed in Table 1. All films were adhesive, passing the Scotch tape test<sup>28</sup> (no particles were peeled off from the substrate), resisted scratching with a steel scalpel<sup>29</sup> and are indefinitely stable in air over several months. The films showed no pin-hole defects and no particulates were observed in the exhaust gas.

X-ray photoelectron spectroscopy (XPS) was used to study the nature and concentration of the phosphorus dopant in TiO<sub>2</sub>. As XPS is a surface-sensitive technique ( $\leq 10$  nm),<sup>30</sup> several depths within the bulk were investigated by etching the surface with argon sputtering. Previous reports have shown that phosphorus can substitutionally enter the TiO<sub>2</sub> as either P<sup>5+</sup> cations that replace Ti<sup>4+</sup> lattice sites or P<sup>3-</sup> anions that replace O<sup>2-</sup> lattice sites, which are commonly assigned to XPS P 2p binding energies of ca. 135 and 129 eV respectively.<sup>18,31-33</sup>

The P-doped TiO<sub>2</sub> films synthesised in this work showed a single surface peak at 133.7 eV, which was assigned to P<sup>5+</sup> cations (**Figure 1**).<sup>18,20</sup> Interestingly, surface etching revealed an additional P 2p environment in the bulk of highly doped samples ( $\geq 2.3$  at.%). This bulk peak at 128.8 eV was assigned to P<sup>3-</sup> anions (**Figure 1**).<sup>33,34</sup> It is known that the etching procedure can change the oxidation state of elements during XPS depth profiling,<sup>35</sup> however, this is unlikely in the hypothetical case of a reduction from P<sup>5+</sup> to P<sup>3-</sup>, since argon sputtering typically encourages oxidation. The fact that solely P<sup>5+</sup> was present at the surface, even in samples that contained both P<sup>5+</sup> and P<sup>3-</sup> in the bulk, was attributed to surface oxidation on exposure to air.

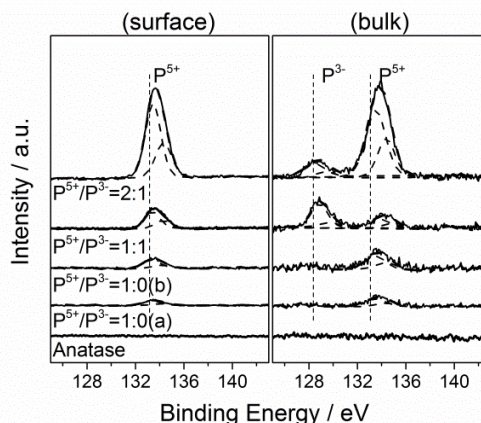


**Figure 1.** XPS spectra of surface (left) and bulk average (right) species in the P 2p environment (assignments included) of P-TiO<sub>2</sub> films (P<sup>5+</sup>/P<sup>3-</sup> = 1:0(a), P<sup>5+</sup>/P<sup>3-</sup> = 1:0(b), P<sup>5+</sup>/P<sup>3-</sup> = 1:1 and P<sup>5+</sup>/P<sup>3-</sup> = 2:1) and as-deposited undoped TiO<sub>2</sub> film used as reference. The solid lines represent experimental data and dotted lines represent the deconvolution of each chemical state into its respective 2 p<sub>3/2</sub> and 2 p<sub>1/2</sub> environments.

**Table 1.** Experimental details for the deposition of undoped and P-doped TiO<sub>2</sub> thin films. The temperature and mass flow conditions were constant for metal (TiCl<sub>4</sub>) and oxygen (C<sub>4</sub>H<sub>8</sub>O<sub>2</sub>) precursors: 341 and 311 K and 6.7 x 10<sup>-3</sup> and 3.1 x 10<sup>-3</sup> g min<sup>-1</sup>, respectively.

Sample	Experimental Details				
	P Bubbler T (K)	P Mass Flow (10 <sup>-3</sup> ) (g min <sup>-1</sup> )	[P] total (at. %)	[P <sup>5+</sup> ] (at. %)	[P <sup>3-</sup> ] (at. %)
Anatase	--	--	--	--	--
P <sup>5+</sup> /P <sup>3-</sup> =1:0(a)	365	0.13	0.50 ± 0.18	0.50 ± 0.18	--
P <sup>5+</sup> /P <sup>3-</sup> =1:0(b)	364	0.24	0.90 ± 0.37	0.90 ± 0.37	--
P <sup>5+</sup> /P <sup>3-</sup> =1:1	355	0.38	2.27 ± 0.58	1.17 ± 0.51	1.10 ± 0.65
P <sup>5+</sup> /P <sup>3-</sup> =2:1	363	0.57	2.98 ± 0.62	2.04 ± 0.68	0.94 ± 0.37

The relevant samples in this work were given a nomenclature based on the approximate relative ratio of P<sup>5+</sup>/P<sup>3-</sup>, as determined by XPS analysis of the P 2p environment. Four distinct P-TiO<sub>2</sub> samples were studied herein (**Table 1**): P<sup>5+</sup>/P<sup>3-</sup> = 1:0(a), P<sup>5+</sup>/P<sup>3-</sup> = 1:0(b), P<sup>5+</sup>/P<sup>3-</sup> = 1:1 and P<sup>5+</sup>/P<sup>3-</sup> = 2:1. The content of phosphorus in these samples was 0.50, 0.90, 2.27 and 2.98 at. %, respectively (**Table 1**).

### 3.2. Structural Properties

X-ray diffraction analysis showed that all undoped and P-doped TiO<sub>2</sub> thin-films comprised purely the anatase phase structure. No traces of the rutile phase or any additional phosphorus-based structures were observed (see Supporting Information Figure (1S)). The diffraction peaks shifted substantially in P-doped samples relative to undoped samples. Patterns were fit to a Le Bail refined model in order to quantify these changes in the lattice. The largest changes were found in the tetragonal *c* axis. The film that contained the lowest level of P doping (P<sup>5+</sup>/P<sup>3-</sup> = 1:0 (a)), showed the most contracted unit cell (135.7 ± 0.08 Å<sup>3</sup>) relative to pure anatase (136.74 ± 0.08 Å<sup>3</sup>). Samples with low levels of P-doping, P<sup>5+</sup>/P<sup>3-</sup> = 1:0(a) (0.50 at.%) and P<sup>5+</sup>/P<sup>3-</sup> = 1:0(b) (0.90 at.%), showed only one P 2p environment, attributed to P<sup>5+</sup> states,<sup>21,26</sup> these P<sup>5+</sup> cations are most likely substituted on Ti<sup>4+</sup> sites. The large contractions in the unit cell were explained in terms of the differences in ionic radii; where 6 coordinate complexes of P<sup>5+</sup> and Ti<sup>4+</sup> show average ionic radii of 0.380 Å and 0.605 Å respectively. In contrast, films with higher levels of P-doping, P<sup>5+</sup>/P<sup>3-</sup> = 1:1 (2.27 at.%) and P<sup>5+</sup>/P<sup>3-</sup> = 2:1 (2.98 at.%), showed two different P 2p environments, attributed to P<sup>5+</sup> and P<sup>3-</sup> states,<sup>18,31-33</sup> where these P<sup>3-</sup> anions most likely substituted O<sup>2-</sup> sites. The contractions in the unit cell were suppressed when both types of P-dopant were present.

This was because the P<sup>3-</sup> states (2.10 Å) that replaced O<sup>2-</sup> sites (1.40 Å) were larger and thus off-set the contractions caused by P<sup>5+</sup> insertion. An additional effect was observed where the preferential growth in particular diffraction planes changed with P-doping level. In a single crystal, growth in the (101) diffraction plane of TiO<sub>2</sub> is most prominent. However, films grown by APCVD tend to show the most substantial increase

in preferred growth in the (211) diffraction plane alongside a suppressed growth in the (101) plane. Nevertheless, Hyett *et al.*<sup>36</sup> found that the photocatalytic activities of TiO<sub>2</sub> films grown by APCVD did not change much with changes in preferred growth. In undoped and P-doped films of low level doping, films showed the most preferred growth in the (211) diffraction plane. At higher levels of P-doping, preferred growth was most prominent in the (101) diffraction plane (see Supporting Information Figure (1S)). A similar trend was also observed by Kafizas *et al.*<sup>17</sup> and Bhachu *et al.*<sup>14</sup> in Nb-doped TiO<sub>2</sub> films grown by APCVD, where the most preferred growth changed from the (101) to the (211) planes at high concentrations of Nb.

Further structural studies were carried out using Raman spectroscopy. The Raman studies confirmed the results observed through X-ray diffraction analysis, as solely anatase phase of TiO<sub>2</sub> was present in all films. The major scattering E<sub>g</sub> band, typically found at 144 cm<sup>-1</sup> in undoped anatase, shifted to lower wavenumbers upon P doping (**Table 2**). The E<sub>g</sub> mode represents phonons operating primarily in the *a*-axis of the tetragonal unit cell.<sup>37</sup> A clear trend is observed between the degree of red-shift in the E<sub>g</sub> band and contraction in unit cell volume (**Table 2**), where the most red-shifted bands were found in the most contracted unit cells (*i.e.* samples P<sup>5+</sup>/P<sup>3-</sup>=1:0(a) and P<sup>5+</sup>/P<sup>3-</sup>=1:0(b)) (See supporting information Figures 2S and 3S).

### 3.3. Film Morphology

Scanning electron microscopy (SEM) analysis was used to investigate the structural morphologies of both undoped and P-doped TiO<sub>2</sub> samples. Undoped TiO<sub>2</sub> films showed well defined shell-shaped aggregated particles (**Figure 2(a)**). However, the incorporation of phosphorus in the structure of the films caused a drastic change in the structural morphology. At low levels of P-doping (sample P<sup>5+</sup>/P<sup>3-</sup> = 1:0(b)), larger particles, more jagged in shape, were observed (**Figure 2(b)**). At high levels of P-doping (P<sup>5+</sup>/P<sup>3-</sup> = 2:1), even larger and more rounded bulb-shaped particles were observed (**Figure 2(c)**). Overall, P-doping increased particle size.

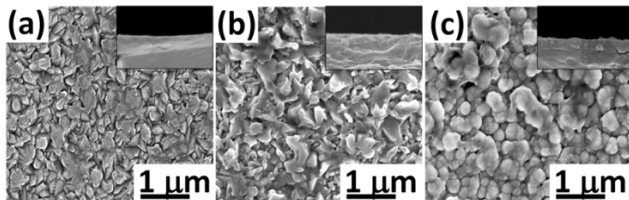
**Table 2.** Physical and functional characterisation data for undoped and P-doped TiO<sub>2</sub> films acquired *via* X-ray diffraction analysis (XRD), Raman spectroscopy, UV/Visible absorption spectroscopy, X-ray photoelectron spectroscopy (XPS), transient absorption spectroscopy (TAS), atomic force microscopy (AFM), photocatalytic degradation of stearic acid (SA) and Van der Pauw and Hall Effect electrical measurements.

Sample	Physical Properties							
	X-ray Diffraction			Spectroscopy			TAS	
	a [Å]	c [Å]	Vol [Å <sup>3</sup> ]	Raman (E <sub>g</sub> )cm <sup>-1</sup>	Band gap (eV)	d [nm min <sup>-1</sup> ] <sup>a</sup>	T % @ 2500 nm <sup>b</sup>	t 1/2 from 2 μs
Anatase	3.787(1)	9.533(6)	136.74(6)	143.9	3.22	305	73.2	58
P <sup>5+</sup> /P <sup>3-</sup> =1:0(a)	3.782(1)	9.505(6)	135.67(4)	141.7	3.36	315	66.8	--
P <sup>5+</sup> /P <sup>3-</sup> =1:0(b)	3.780(1)	9.492(5)	135.93(8)	141.4	3.39	350	67.3	14
P <sup>5+</sup> /P <sup>3-</sup> =1:1	3.785(2)	9.520(6)	136.39(6)	143.2	3.28	385	72.3	3.1
P <sup>5+</sup> /P <sup>3-</sup> =2:1	3.788(1)	9.512(2)	136.53(3)	142.7	3.24	450	74.8	19

	Functional properties			Electrical properties		
	AFM	Photocatalysis		Hall effect probe		
	Surface area (μm <sup>2</sup> )	FQE (10 <sup>-4</sup> )	FQY (10 <sup>-4</sup> )	ρ (Ω cm)	μ (cm <sup>2</sup> V <sup>-1</sup> s <sup>-1</sup> )	n (10 <sup>19</sup> cm <sup>-3</sup> )
Anatase	29.35 ± 0.39	0.86 ± 0.01	1.34 ± 0.02	--	--	--
P <sup>5+</sup> /P <sup>3-</sup> =1:0(a)	--	0.33 ± 0.01	0.65 ± 0.02	1.69 ± 0.42	0.81 ± 0.13	0.49 ± 0.21
P <sup>5+</sup> /P <sup>3-</sup> =1:0(b)	29.00 ± 0.18	0.47 ± 0.02	0.78 ± 0.03	--	--	--
P <sup>5+</sup> /P <sup>3-</sup> =1:1	--	0.01 ± 0.01	0.01 ± 0.01	8.18 ± 2.13	0.10 ± 0.04	2.21 ± 1.76
P <sup>5+</sup> /P <sup>3-</sup> =2:1	30.13 ± 0.57	0.55 ± 0.02	0.82 ± 0.02	6.49 ± 1.89	0.09 ± 0.05	1.54 ± 1.11

<sup>a</sup>d = film thickness; <sup>b</sup>average between 0 and 2500 nm. Numbers in parentheses represent the error on the last digit.



**Figure 2.** Scanning electron microscopy (SEM) images of typical (a) undoped TiO<sub>2</sub>, (b) low concentration and (c) high concentration P-TiO<sub>2</sub> films. The inset shows side-view SEM of the films.

Further inspection using atomic force microscopy (AFM) was performed six times locally for each sample. Scan areas of 5 μm × 5 μm were sampled with a 20 nm special frequency using a contact (PeakForce) scanning mode. The roughness induced surface area increase was calculated by averaging the projected surface areas for each of the samples. In line with SEM studies, progressively larger and more rounded particles were observed upon P-doping (**Figure 3**). The root mean squared roughness increased significantly from 16 nm for undoped TiO<sub>2</sub> to 51 nm for high levels of P doping, however, the projected surface area saw only a slight increase (from 29.4 μm<sup>2</sup> to 30.1 μm<sup>2</sup>) as the peaks became more sparse.

However, the calculated surface areas ranged from just 29.35 ± 0.39 μm<sup>2</sup> in undoped TiO<sub>2</sub> films, to 29.00 ± 0.18 μm<sup>2</sup> and 30.13 ± 0.63 μm<sup>2</sup> in P<sup>5+</sup>/P<sup>3-</sup>=1:0(b) and P<sup>5+</sup>/P<sup>3-</sup>=2:1 samples, respectively (**Table 2**).

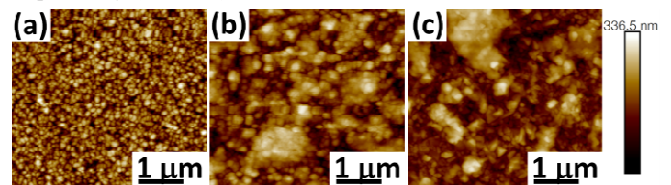


**Figure 3.** Atomic force microscopy (AFM) images of typical (a) undoped TiO<sub>2</sub> and P-doped TiO<sub>2</sub> films, with (b) low levels of phosphorus (P<sup>5+</sup>/P<sup>3-</sup> = 1:0 (0.90 at. %)) and (c) high levels of phosphorus (P<sup>5+</sup>/P<sup>3-</sup> = 2:1 (2.98 at. %)).

### 3.4. Optical Properties

The undoped TiO<sub>2</sub> thin-films produced in this work were highly transparent. The incorporation of low P concentrations (< 1 at.%) resulted in films with a blue/yellow tinge, evidenced by a slight dip in transmission in the green-red absorption region from ≈ 600 to 2000 nm (**Figure 4**). Indeed, Tauc plot analysis (**Figure 4, inset**) showed a slight shift in absorption into the blue region for these P-TiO<sub>2</sub> samples, with band-gap energies estimated around 3.4 eV compared to undoped films (~3.2

eV). Surprisingly, doped films with P high content (> 1 at.%) did not show this blue shift and the corresponding band-gap energies were comparable to undoped TiO<sub>2</sub>. The change in band-gap energy was discussed in terms of the different properties of the two oxidation states of phosphorus (P<sup>5+</sup> and P<sup>3+</sup>) in the TiO<sub>2</sub> structure. The increase in band-gap energy was only observed for films containing low concentrations of phosphorus and only P<sup>5+</sup> cations. This increase would certainly not be expected from the incorporation of P<sup>3+</sup> anions into O<sup>2-</sup> lattice sites. The density of states of TiO<sub>2</sub> is primarily composed of O 2p orbitals in the valence band and Ti 3d orbitals in the conduction band. Anionic dopants, such as P<sup>3-</sup>, typically replace O<sup>2-</sup> sites and thus alter primarily the valence band of TiO<sub>2</sub>. This is the case of N<sup>3-</sup> dopants, for instance, which occupy O<sup>2-</sup> sites, and then mixing of N 2p and O 2p orbitals pushes the valence band upwards, thus causing a *decrease* in band-gap energy (*i.e.* red-shift of absorption spectrum).<sup>6,38,39</sup> One might attribute this to a Moss-Burstein shift that occurs when the carrier concentration is high enough to cause degeneracy and raise the conduction band minimum by occupancy. However, as discussed below, Hall Effect probe measurements showed that the charge carrier concentrations were very low when merely P<sup>5+</sup> was present ( $n \approx 5 \times 10^{18} \text{ cm}^{-3}$ ) compared to those recorded at high P levels ( $1 \times 10^{19} \leq n \leq 5 \times 10^{19} \text{ cm}^{-3}$ ), where both P<sup>5+</sup> and P<sup>3+</sup> were presented. If a Moss-Burstein shift was the reason for a blue-shift in band-gap energy, then the same phenomenon should also have been observed in the case of the latter samples. Another possibility is that these differences in band-gap were due to changes in unit cell volume. As inferred from our XRD analysis, little or no disruption of the lattice was found in samples containing both P<sup>5+</sup> and P<sup>3+</sup>, whilst samples containing P<sup>5+</sup> species only resulted in unit cell expansion, greater average distance between the ions within the lattice and thus widened density of states. The intrinsic disorder caused by having a significant proportion of both P<sup>5+</sup> and P<sup>3+</sup> anions in the structure could also have an impact on the measure band gaps. At present the exact origin of these band gaps trends remains unanswered.

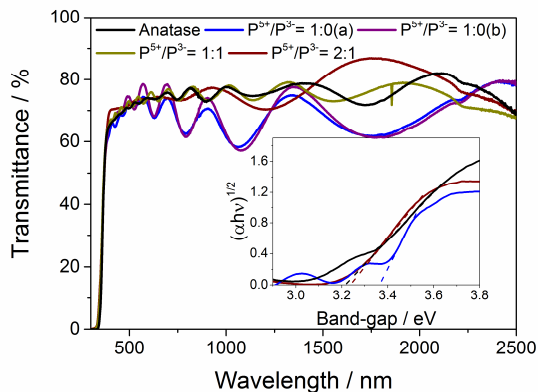


**Figure 4.** UV-Vis spectra of selected P-TiO<sub>2</sub> films (P<sup>5+</sup>/P<sup>3-</sup> = 1:0(a), P<sup>5+</sup>/P<sup>3-</sup> = 1:0(b), P<sup>5+</sup>/P<sup>3-</sup> = 1:1 and P<sup>5+</sup>/P<sup>3-</sup> = 2:1). Undoped TiO<sub>2</sub> (black solid line) is included for reference. The inset shows band-gap measurements derived from Tauc plot analysis for P-doped films with low P levels, P<sup>5+</sup>/P<sup>3-</sup> = 1:0(a) (burgundy line) and high P levels, P<sup>5+</sup>/P<sup>3-</sup> = 2:1 (blue line). The black line in the inset corresponds to undoped TiO<sub>2</sub>.

Transient absorption spectroscopy (TAS) measurements on the microsecond to second time-scale were used to investigate the lifetime and population of photo-generated charge carriers in both undoped and P-doped samples (**Figure 5**). Transient absorption spectroscopy (TAS) is a form of laser flash spectroscopy that tracks transient changes in absorption after an excitation pulse. In many semiconductor photocatalysts, these transient changes in absorption have been shown to be directly related to transient changes in photo-generated charge.<sup>40-42</sup> It has been shown that the population and dynamics of photo-generated electrons or holes could be studied in TiO<sub>2</sub> by tracking transient absorbance changes at particular wavelengths.<sup>43</sup> Measurements were conducted in argon (an inert environment), which meant the photo-generated charges could only recombine (*i.e.* no photocatalytic processes could occur). As the photo-generated charges recombined, the change in transient absorption decreased towards zero net change (*i.e.* complete recombination of charge). The speed at which recombination occurs dictates the natural lifetime of photo-generated charge in a given material. In undoped anatase TiO<sub>2</sub>, photo-generated charges naturally recombine within 100 ms and show a power law decay typical of the trap/ de-trapping movement of charge.<sup>24</sup> Each TAS spectrum was measured from the  $\mu\text{s}$  to s timescale, which misses the stage of initial charge generation and trapping (fs to ps timescale) but covers the timescale where most photocatalytic processes typically occur such as the reduction of O<sub>2</sub>,<sup>44</sup> the oxidation of NO<sup>45</sup> and the oxidation of water.<sup>46</sup>

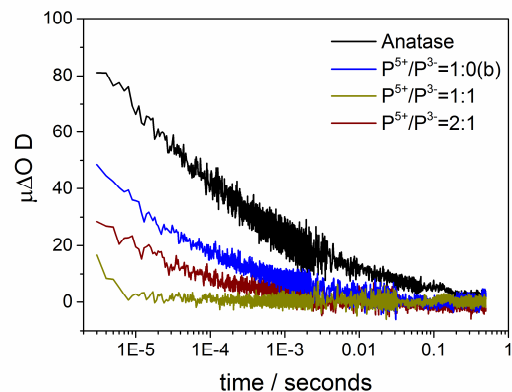


**Figure 5.** Transient absorption kinetic decays on the microsecond to second time-scale, normalised at 2  $\mu\text{s}$ , was used to investigate the lifetimes of photogenerated charge carriers for undoped (black line) and P-doped TiO<sub>2</sub> films (P<sup>5+</sup>/P<sup>3-</sup> = 1:0(b), blue line; P<sup>5+</sup>/P<sup>3-</sup> = 1:1, green line; and P<sup>5+</sup>/P<sup>3-</sup> = 2:1, burgundy line).

A 355 nm laser pulse was used to excite our samples, creating photo-generated charges in the semiconductor alongside a transient change in absorption (**Figure 5**). Our series of samples had similar levels of absorption at 355 nm (**Figure 4**), which allowed us to also compare changes in population. At 2  $\mu\text{s}$ , the undoped TiO<sub>2</sub> sample possessed the highest absorbance. This meant that more photo-generated charges were

present in this material at this time-scale compared with the P-doped samples, even though all samples would have absorbed a similar level of light from the laser pulse. Moreover, when we compared the time it took for the initial absorption signal at 2  $\mu\text{s}$  to decrease to half of its initial value ( $t_{1/2}$ ) it was observed that recombination was slowest in the undoped sample (**Table 2**). Undoped anatase  $\text{TiO}_2$  possessed the longest lifetime with a  $t_{1/2}$  of 58  $\mu\text{s}$ . The next longest lived charges were found in samples  $\text{P}^{5+}/\text{P}^{3-}=2:1$  and  $\text{P}^{5+}/\text{P}^{3-}=1:0$ (b), with a  $t_{1/2}$  of 19 and 14  $\mu\text{s}$  respectively. The shortest lived photo-generated charge was found in sample  $\text{P}^{5+}/\text{P}^{3-}=1:1$ , with a  $t_{1/2}$  of 3.1  $\mu\text{s}$ .

Overall, a general trend was observed where P-doping decreased the lifetime of photo-generated charge in  $\text{TiO}_2$ . It is often argued that doping  $\text{TiO}_2$  typically encourages recombination, where the dopant sites act as centres for recombination.<sup>47</sup> Interestingly, the rate of recombination varied substantially in our P-doped  $\text{TiO}_2$  materials. No complete correlation between recombination rate and P-doping levels could be established; however our findings do suggest that a faster recombination rate occurs when the  $\text{P}^{5+}$  and  $\text{P}^{3-}$  concentration are equivalent.

### 3.5. Functional Properties

#### Electrical Properties: Hall Effect Probe

Electrical properties of P-doped  $\text{TiO}_2$  films were investigated by room temperature Hall Effect probe measurements in the van der Pauw configuration on samples made with soldered indium-tin contacts. Several areas in each of the low, mid and high dopant level in P- $\text{TiO}_2$  were examined and area-specific XPS data obtained. Figure 6 shows median values and standard error for carrier mobility, carrier density and resistivity of the P- $\text{TiO}_2$  films as a function of overall P-dopant and relative presence of  $\text{P}^{3-}$ . All P- $\text{TiO}_2$  films display n-type conductivity, with different electrical conductivity effects depending on the oxidation state of the dopant ( $\text{P}^{5+}$  and  $\text{P}^{3-}$ ). Furthermore, the dopant seems to induce different electrical conductivity effects depending on oxidation state; the presence of the  $\text{P}^{3-}$  state (substituting the  $\text{O}^{2-}$  lattice site and neutralising an electron in the system) corresponds to a decrease in both resistivity and charge carrier density whilst the  $\text{P}^{5+}$  state (substituting on the  $\text{Ti}^{4+}$  site and liberating an electron) effects an increase in electrical conductivity. Only at low phosphorous doping levels is the  $\text{P}^{5+}$  state present alone ( $< 1$  at.%), whereas at higher doping levels (from  $\approx 2$  at.%) the  $\text{P}^{3-}$  state is also detectable.

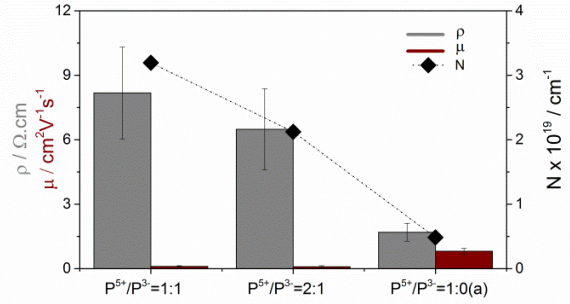


**Figure 6.** A comparison of Hall Effect probe measured resistivity (grey bars), charge carrier mobility (burgundy bars) and carrier density (full diamonds) for P-doped  $\text{TiO}_2$  thin films;  $\text{P}^{5+}/\text{P}^{3-}=1:1$ ,  $\text{P}^{5+}/\text{P}^{3-}=2:1$  and  $\text{P}^{5+}/\text{P}^{3-}=1:0$ (a). Standard errors are included for median electrical property values.

The dramatic increase in charge carrier density values indicate that effective P-doping induces a crossover into semiconductor degeneracy, achieving a more ‘metallic’ character in accordance with the Mott metal-to-insulator transition. Such carrier concentration levels are not achievable in nominally undoped  $\text{TiO}_2$  films that allow conduction through oxygen vacancies. The carriers are thought to transfer *via* a band process. Carrier density shows a typical transition from high resistivity, to low resistivity at an idealised dopant level ( $\approx 1$  at. %), followed again by an increase in resistivity. This can be rationalised by considering the role of P dopants in  $\text{TiO}_2$ . At low doping levels P will enter the lattice in the Ti site, with an oxidation state of  $5+$ . The ionic radius of six coordinated  $\text{P}^{5+}$  at 0.380  $\text{\AA}$  is smaller than that of  $\text{Ti}^{4+}$  (0.605  $\text{\AA}$ ), so it will readily fit in that Ti lattice position.  $\text{P}^{3-}$ , however, is much larger than  $\text{O}^{2-}$ , and so will not be incorporated as readily into  $\text{TiO}_2$ . As the concentration of dopant is increased, the formation energy of the cationic dopant, which acts as a shallow donor and is in the  $\text{P}_{\text{Ti}}^{+1}$  charge state (**Figure 7**), increases over the range of the band gap. P on an oxygen site, however, acts as a p-type dopant, with the hole state localized on the p-states of the P dopants. At high Fermi levels, however,  $\text{P}_{\text{O}}^{-1}$  will start to become favourable. Once the concentrations of P dopant exceeds  $\sim 1\%$ , the  $\text{P}_{\text{O}}^{-1}$  starts to dominate, acting as a hole killer, and pinning the Fermi level above just the conduction band minimum (CBM). Any further increase of the P doping concentration will just result in the decrease of the number of electrons in the system.

Whilst the effective carrier density values are fairly impressive;  $0.5 - 2.2 \times 10^{19} \text{ cm}^{-3}$  (especially as compared to other non-metal dopants such as fluorine), the carrier mobilities were low ( $\approx 0.1 - 0.8 \text{ cm}^2\text{V}^{-1}\text{s}^{-1}$ ) and attributed to ionised impurity scattering. Overall, the current effective resistivities (of the order of  $10^0 \text{ }\Omega\cdot\text{cm}$ ) were too high for conventional TCO applications.

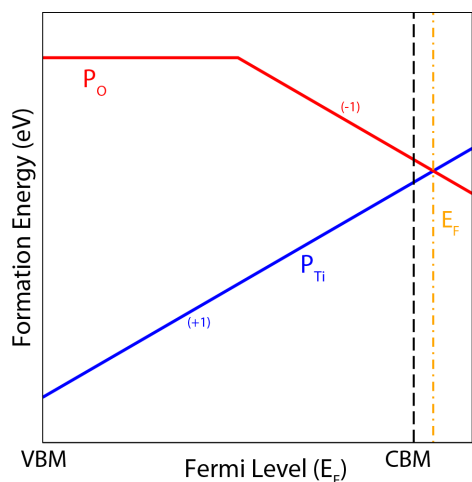
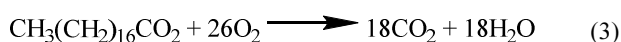


**Figure 7.** Schematic showing the mechanism of dopant self-compensation as the P-doping level is increased. The y-axis displays the formation energy of the defect species, and the x-axis shows the position of the Fermi level relative to the VBM and CBM for anatase TiO<sub>2</sub>. For high doping levels (above the CBM), the Fermi level gets trapped (Orange dot-dash vertical line) by the formation of P<sub>O</sub><sup>-1</sup>.

The marked decrease in mobility with phosphorous doping demonstrates the heavy ionised impurity scattering effect (whether direct or indirect) of the dopant. However, the presence of the P<sup>3-</sup> state correlates with a larger decrease in carrier mobility. Indeed, whether the decrease in mobility is a result of the higher presence of the phosphorous dopant (which leads to the presence of P<sup>3-</sup> above a threshold value) or to the anionic state itself is difficult to distinguish. However, our findings suggest that at similar levels of total P-doping, a greater relative presence of the P<sup>3-</sup> state vs. the P<sup>5+</sup> state will result in a more severe decrease in mobility.

#### Photocatalytic Activity

The experimental observations reported on the photocatalytic activity of P-TiO<sub>2</sub> materials are very different. Typical synthesis methods, such as sol-gel, may produce materials with varying phosphate content and surface area, potentially affecting the performance of P-TiO<sub>2</sub> photocatalysts.<sup>18-21</sup> In contrast, APCVD allowed the synthesis of films with homogeneous P content across the bulk and also comparable surface properties. The synthesized films also allowed a thorough study of the correlation of P species and the photocatalytic properties of these materials. The photocatalytic activity of the P-TiO<sub>2</sub> films was evaluated during the degradation of stearic acid under UVA irradiation (1.2 mW cm<sup>-2</sup>).<sup>25</sup> The overall photocatalytic reaction is given by Equation 3.



The photocatalytic process was monitored using FTIR, following the disappearance of characteristic C-H modes of the acid (2958, 2923 and 2853 cm<sup>-1</sup>). The photocatalytic rates were

estimated from linear regression of the initial steps (30 – 40 %) of the curve of integrated area vs. illumination time. The corresponding rates were expressed as formal quantum efficiencies (FQE), defined as molecules of stearic acid degraded over incident photons (units, molec x photon<sup>-1</sup>) (**Figure 8**). The variation in FQE values was discarded to be due to differences in physical properties of the films, since all films investigated showed comparable thicknesses and crystallinity, based on XRD and Raman analysis (see supporting information), as well as similar surface topography (**Figures 2 and 3, Table 2**). With the exception of sample P<sup>5+</sup>/P<sup>3-</sup>=1:1, which showed no activity, most P-TiO<sub>2</sub> films showed moderate activities compared to undoped TiO<sub>2</sub> samples. This is surprising for highly conductive samples, since electrical conductivity is usually observed in detriment of photocatalytic activity.<sup>13</sup> It is also worth noting that previous groups have observed far greater detriment when doping with nitrogen or sulphur.<sup>36,48</sup>

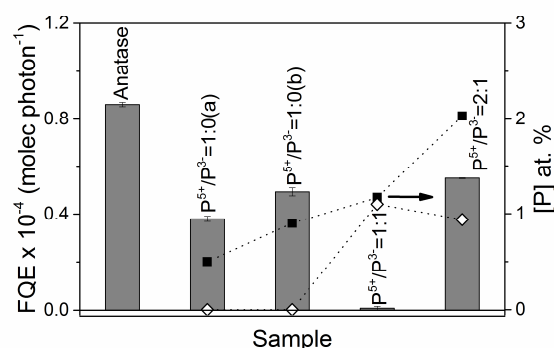


**Figure 8.** Formal quantum efficiencies obtained during photo-degradation of stearic acid under UVA irradiation of selected P-TiO<sub>2</sub> films and undoped TiO<sub>2</sub> film, used as reference. The relative levels (%) of cation phosphorus (P<sup>5+</sup>, full squares) and anion phosphorus (P<sup>3-</sup>, empty diamonds) are indicated for comparison.

The film photocatalytic activities (**Figure 8**) could be correlated directly with photo-generated charge carrier lifetimes (**Figure 5**), where high lifetime resulted in high photocatalytic activity, undoped TiO<sub>2</sub> being the most active sample (FQE = 0.86 molec.photon<sup>-1</sup>;  $t_{1/2}$  = 58  $\mu$ s), followed by P<sup>5+</sup>/P<sup>3-</sup> = 2:1, P<sup>5+</sup>/P<sup>3-</sup> = 1:0(b) and P<sup>5+</sup>/P<sup>3-</sup> = 1:0(a) doped films (FQE = 0.55, 0.47 and 0.33 molec.photon<sup>-1</sup>;  $t_{1/2}$  = 19, 14 and *na*  $\mu$ s, respectively). Sample P<sup>5+</sup>/P<sup>3-</sup> = 1:1 showed the lowest lifetime ( $t_{1/2}$  = 3.1  $\mu$ s) and no photocatalytic activity. These observations were attributed to the kinetics of the typical processes associated with photocatalysis on TiO<sub>2</sub>. It is generally accepted that photocatalysis on TiO<sub>2</sub> proceeds through two avenues: (i) the reaction of holes with surface H<sub>2</sub>O forming highly reactive hydroxyl radicals that subsequently degrade nearby organics or (ii) the reaction of electrons with O<sub>2</sub> forming highly reactive superoxide species that can also degrade nearby organics.<sup>1</sup> These two processes occur on different time-scales, where it has been shown that (i) holes can react with H<sub>2</sub>O within 2  $\mu$ s and (ii) electrons react with O<sub>2</sub> from 10 – 900  $\mu$ s.<sup>49</sup> Our TAS studies showed that the sample with longest-lived photo-



generated charge was undoped TiO<sub>2</sub>. However, from just 2 – 58 μs, half of those charges had recombined. Given the slow reaction of electrons with O<sub>2</sub>, we attribute the low efficiency in the photocatalytic degradation of stearic acid (≈ 1.4 %) to the predominance of recombination vs. O<sub>2</sub> reduction.

Interestingly, samples with a predominant presence of P<sup>5+</sup> showed high photocatalytic activity and electrical conductivity, whilst an equivalent presence of P<sup>3-</sup> and P<sup>5+</sup> resulted in inactive samples with negligible conductivity. The latter observation was attributed to the promotion of electron-hole recombination in P<sup>3-</sup> sites (see Supporting Information Figure 5S), where the photo-generated charge rate in the most P<sup>3-</sup>-rich sample (P<sup>5+</sup>/P<sup>3-</sup>=1:1) decayed almost 20 times faster than that observed for undoped TiO<sub>2</sub> films (**Figure 5**).

#### 4. CONCLUSIONS

A new strategy to synthesise P-doped TiO<sub>2</sub> films (either P<sup>5+</sup> doped or P<sup>5+</sup> and P<sup>3-</sup> doped) using atmospheric pressure chemical vapour deposition (APCVD) has been presented. This is, to the best of our knowledge, the first example of APCVD synthesis to incorporate anionic phosphorus (P<sup>3-</sup>) in TiO<sub>2</sub>.

Transient absorption spectroscopy (TAS) showed an overall decrease of photogenerated charge carrier lifetimes upon the incorporation of phosphorus in TiO<sub>2</sub>, particularly in the case of P<sup>3-</sup> species. The impact of P groups was also consistent with a decrease in photocatalytic activity, evaluated during the mineralisation of stearic acid. It was concluded that P<sup>3-</sup> species contributed to a fast recombination of photo-generated charges, which was as high as 20 times faster in the most P<sup>3-</sup>-rich sample compared to the typical rates observed in undoped TiO<sub>2</sub> films and almost 6 times faster than corresponding P<sup>5+</sup>-rich samples.

In addition, Hall Effect probe measurements showed that electrical conductivity was highest in samples rich in P<sup>5+</sup> species as well. This is a significant result, since electrical conductivity often arises to the detriment of photocatalytic activity, and it means a step forward in the formation of novel multifunctional materials, with an optimal balance between self-cleaning and TCO properties – the frontier application of photocatalytic transparent conductors.

#### ASSOCIATED CONTENT

The Supporting Information document shows physical properties of the as-deposited films, X-ray Diffraction (Figure 1S) and Raman analysis (Figure 2S). Photocatalytic degradation of stearic acid under UVA light, infrared spectra and integrated areas, is shown in Figure 4S. A comparison between TAS analysis and degradation of stearic acid is shown in Figure 5S. This material is available free of charge via the Internet at <http://pubs.acs.org/>.

#### AUTHOR INFORMATION

##### Corresponding Author

\*University College London, Dept. Chemistry, Christopher-Ingold Laboratories, 20 Gordon St., London, WC1H 0AJ, United Kingdom. E-mail: [i.p.parkin@ucl.ac.uk](mailto:i.p.parkin@ucl.ac.uk) (I.P. Parkin), Tel.: +44 020 7679 4669; fax: +44 020 7679 7463

#### ACKNOWLEDGMENT

European Commission FP7 is thanked for funding (PCATDES, Grant N.309846). Dr. Chris Blackman is thanked for useful discussion. Dr. Robert Palgrave is thanked for his assistance in the XPS analysis. Dr. Steven Firth and Mr. Kevin Reeves are also thanked for access to the SEM and Raman instruments.

#### ABBREVIATIONS

APCVD, atmospheric pressure chemical vapor deposition; TCO, transparent conducting oxides; XRD, X-ray diffraction; SEM, scanning electron microscopy; AFM, atomic force microscopy; XPS, X-ray photoelectron spectroscopy; TAS, transient absorption spectroscopy.

#### REFERENCES

- (1) Mills, A.; Le Hunte, S. *J. Photochem. Photobio. A Chem.* **1997**, 108, 1.
- (2) Dunnill, C. W. H.; Aiken, Z. A.; Pratten, J.; Wilson, M.; Morgan, D. J.; Parkin, I. P. *J. Photochem. Photobio. A Chem.* **2009**, 207, 244.
- (3) Page, K.; Palgrave, R. G.; Parkin, I. P.; Wilson, M.; Savin, S. L. P.; Chadwick, A. V. *J. Mater. Chem.* **2007**, 17, 95.
- (4) Kafizas, A.; Kellici, S.; Darr, J. A.; Parkin, I. P. *J. Photochem. Photobio. A Chem.* **2009**, 204, 183.
- (5) Korosi, L.; Oszko, A.; Galbacs, G.; Richardt, A.; Zollmer, V.; Dekany, I. *Appl. Catal., B.* **2007**, 77, 175.
- (6) Asahi, R.; Morikawa, T.; Ohwaki, T.; Aoki, K.; Taga, Y. *Science.* **2001**, 293, 269.
- (7) Emeline, A.; Kuznetsov, V. N.; Rybchuk, V. K.; Serpone, N. *Int. J. Photoenergy* **2008**, 2008, 1.
- (8) Zaleska, A. *Recent. Pat. Eng.*, **2008**, 2, 157.
- (9) Viswanathan, B.; Krishanmurthy, K. R. *Int. J. Photoenergy* **2012**, 2012, 1.
- (10) Zhang, J.; Wu, Y.; Xing, M.; Leghari, S. A. K.; Sajjad, S. *Energy Environ. Sci.* **2010**, 3, 715.
- (11) Asahi, R.; Morikawa, T. *Chem. Phys.* **2007**, 339, 57.
- (12) Asahi, R.; Morikawa, T.; Hazama, H.; Matsubara, M. *J. Phys. Condens. Matter.* **2008**, 20, 064227.
- (13) Kafizas, A.; Noor, N.; Carmichael, P.; Scanlon, D. O.; Carmalt, C. J.; Parkin, I. P. *Adv. Funct. Mater.* **2013**, 24, 1758.
- (14) Bhachu, D.; Sathasivam, S.; Sankar, G.; Scanlon, D. O.; Cibin, G.; Carmalt, C. J.; Parkin, I. P.; Watson, G. W.; Bawaked, S. M.; Obaid, A. Y.; Al-Thabaiti, S.; Basahel, S. N. *Adv. Funct. Mater.* **2014**, 24, 5075.
- (15) Gillispie, M. A.; van Hest, M. F. A. M.; Dabney, M. S.; Perkins, J. D.; Ginley, D. S. *J. Mater. Res.* **2007**, 22, 2832.
- (16) Hitosugi, T.; Yamada, N.; Nakao, S.; Hirose, Y.; Hasegawa, T. *Phys. Status Solidi A.* **2010**, 7, 1529.
- (17) Kafizas, A.; Noor, N.; Carmalt, C. J.; Parkin, I. P. *J. Mater. Chem. C.* **2013**, 1, 6335.
- (18) Yu, J. C.; Zhang, L.; Zheng, Z.; Zhao, J. *Chem. Mater.* **2003**, 15, 2280.
- (19) Li, F.; Jiang, Y.; Xia, M.; Sun, M.; Xue, B.; Liu, D.; Zhang, X. *J. Mater. Chem. C.* **2009**, 113, 18134.
- (20) Korosi, L.; Papp, S.; Bertoti, I.; Dekany, I. *Chem Mater.* **2007**, 19, 4811.
- (21) Gopal, N. O.; Lo, H.; Ke, T.; Lee, C.; Chou, C.; Wu, J.; Sheu, S.; Ke, S. *J. Phys. Chem. C* **2012**, 116, 16191.
- (22) O'Neill, S. A.; Parkin, I. P.; Clark, R. J. H.; Mills, A.; Elliott, N. *J. Mater. Chem.* **2003**, 13, 56.

- (23) Swanepoel, R. *J. Phys. E: Instrum.* **1983**, 16, 1214.
- (24) Cowan, A. J.; Tang, J.; Leng, W.; Durrant, J. R.; Klug, D. R. *J. Phys. Chem. C* **2010**, 114, 4208.
- (25) Mills, A.; Wang, J. *J. Photochem. Photobiol. A Chem.* **2006**, 182, 181.
- (26) Evans, P.; Pemble, M. E.; Sheel, D. W. *Chem. Mater.* **2006**, 18, 5750.
- (27) Kafizas, A.; Parkin, I. P. *J. Am. Chem. Soc.* **2011**, 133, 20458.
- (28) Mittal, K. L. *Electrocomp. Sci. Tech.* **1976**, 3, 21.
- (29) Buttler, D. W.; Stoddart, C. T. H.; Stuart, P. R. *J. Phys. D: Appl. Phys.* **1970**, 3, 877.
- (30) Powell, C. J.; Jablonski, A.; Tilinin, I. S.; Tanuma, S.; Penn, D. R. *J. Electron Spectros. Relat. Phenomena.* **1999**, 98-99, 1.
- (31) Splinter, S. J.; Rofagha, R.; McIntyre, N. S.; Erb, U. *Surf. Interface Anal.* **1996**, 24, 181.
- (32) Lin, L.; Lin, W.; Xie, J. L.; Zhu, Y. X.; Zhao, B. Y.; Xie, Y. C. *Appl. Catal., B* **2007**, 75, 52.
- (33) Blackman, C.; Carmalt, C. J.; Parkin, I. P.; O'Neill, S. *Chem. Mater.* **2002**, 14, 3167.
- (34) Myers, C. E.; Franzen, H. F.; Anderegg, J. W. *Inorg. Chem.* **1985**, 24, 1822.
- (35) Seah, M. P. *Surf. Interface Anal.* **1980**, 2, 222.
- (36) Hyett, G.; Green, M.; Parkin, I. P. *J. Am. Chem. Soc.* **2006**, 128, 12147.
- (37) Ohsaka, T.; Izumi, F.; Fujiki, Y. *J. Raman Spectrosc.* **1978**, 7, 321.
- (38) Yates, H. M.; Nolan, M. G.; Sheel, D. W.; Pemble, M. E. *J. Photochem. Photobiol., A* **2006**, 179, 213.
- (39) Finazzi, E.; Di Valentin, C.; Selloni, A.; Pacchioni, G. *J. Phys. Chem. C* **2007**, 111, 9275.
- (40) Pesci, F. M.; Cowan, A. J.; Alexander, B. D.; Durrant, J. R.; Klug, D. R. *J. Phys. Chem. Lett.* **2011**, 2, 1900.
- (41) Pendlebury, S. R.; Wang, X.; Le Formal, F.; Cornuz, M.; Kafizas, A.; Tilley, S. D.; Gratzel, M.; Durrant, J. R. *J. Am. Chem. Soc.* **2014**, 136, 9854.
- (42) Ma, Y.; Pendlebury, S. R.; Reynal, A.; Le Formal, F.; Durrant, J. R. *Chem. Sci.* **2014**, 5, 2964.
- (43) Fujishima, A.; Zhang, X.; Tryk, D. *Surf. Sci. Rep.* **2008**, 63, 515.
- (44) Peiro, A. M.; Colombo, C.; Doyle, G.; Nelson, J.; Mills, A.; Durrant, J. R. *J. Phys. Chem. B* **2006**, 110, 23255.
- (45) Devahasdin, S.; Fan, C.; Li, K.; Chen, D. H. *J. Photochem. Photobiol. A Chem.* **2003**, 156, 161.
- (46) Tang, J.; Durrant, J. R.; Klug, D. R. *J. Am. Chem. Soc.* **2008**, 130, 13885.
- (47) Kafizas, A.; Parkin, I. P. *J. Mater. Chem.* **2010**, 20, 2157.
- (48) Dunnill, C. W.; Aiken, Z. A.; Pratten, J.; Wilson, M.; Parkin, I. P. *Chem. Vap. Depos.* **2010**, 16, 50.
- (49) Yamakata, A.; Ishibashi, T.; Onishi, H. *J. Phys. Chem. B* **2001**, 105, 7258.

Authors are required to submit a graphic entry for the Table of Contents (TOC) that, in conjunction with the manuscript title, should give the reader a representative idea of one of the following: A key structure, reaction, equation, concept, or theorem, etc., that is discussed in the manuscript. Consult the journal's Instructions for Authors for TOC graphic specifications.

Insert Table of Contents artwork here

